

ARTICLE OPEN



Thermophysical properties of a Si₅₀Ge₅₀ melt measured on board the International Space Station

Yuansu Luo¹✉, Bernd Damaschke¹, Georg Lohöfer² and Konrad Samwer¹

Thermophysical properties of highly doped Si₅₀Ge₅₀ melt were measured contactlessly in the electromagnetic levitation facility ISS-EML on board the International Space Station. The sample could be melted, overheated by about 375 K, and cooled down in 350 mbar Argon atmosphere. A large undercooling of about 240 K was observed and a quasi-homogeneous nucleation on the droplet surface occurred. During the cooling phase, high-resolution videos were taken from the side and the top. The density and thermal expansion were evaluated with digital image processing; the viscosity and the surface tension were measured by means of the oscillating drop technique. Inductive measurements of the electrical resistivity were conducted by a dedicated electronics. All data were taken as a function of temperature T from the overheated melt down to the undercooled range. We found a nonlinear thermal expansion, suggesting a many body effect in the liquid beyond the regular pair interaction, an enhanced damping of surface oscillations likely related to an internal turbulent flow, and an increment of the electrical resistivity with decreased T in the undercooled range regarding a demixing of the components.

npj Microgravity (2020)6:10; <https://doi.org/10.1038/s41526-020-0100-5>

INTRODUCTION

The semiconductors Si and Ge have been the workhorses for electronic hardware production for a long period of time. In addition, Si-Ge alloys and heterostructures using these alloys have come in the focus of interest due to their flexible electronic properties^{1–4}. For productions and applications of materials, the knowledge of thermophysical properties of the melt is essential and they have to be measured accurately. For this purpose we started the ESA-project “SEMITHERM” (“Investigations of thermophysical properties of liquid semiconductors in the melt and the undercooled state under microgravity conditions”, ESA-AO-2000-068). The goals of the project include the precision measurements of the density, thermal expansion, surface tension, viscosity, and electrical resistivity of the liquid Ge and alloys Si_{1–x}Ge_x ($x = 0.75, 0.5, \text{ and } 0.25$). Due to the strong reactivity of the high-temperature melts the experiments need to be performed contactlessly under low-gravity conditions. The Electromagnetic Levitator (ISS-EML) on board of the International Space Station (ISS) is the instrument of choice. For the preparation of these experiments, measurements on parabolic flights have been performed in a similar low-gravity electromagnetic levitation facility (TEMPUS)⁵. The results for Ge-rich Si-Ge alloys have been reported in a previous paper⁶.

Here we report about the measurements with an Si₅₀Ge₅₀ sample on board the ISS. Reports about other concentrations will follow. First, we give an overview of the general processing of the sample, followed by the presentation of the results of measurements of the viscosity, surface tension, density, thermal expansion, and electrical conductivity. All properties were measured in the melt as a function of temperature. In the last section an overview of the EML facility, the experimental details including the sample properties is given.

RESULTS AND DISCUSSION

Melting, cooling, undercooling, and solidification behavior
Eleven melting and cooling cycles of the Si₅₀Ge₅₀ sample (always the same sample) were successfully carried out on board the ISS. Table 1 gives an overview of the processing designed for each cycle, including values of overheat, achieved undercooling and cooling rates (in 350 mbar Ar) above and below the liquidus temperature T_l (1548 K). The overheat is about 375 K in average. Undercooling of about 45 ± 10 K was obtained from cycles #1–#5, jumping to 155 K in cycle #6 and then gradually rising up to 240 K for cycle #11. The result observed arises possibly from gradual melting of the surface oxide SiO₂ at T_{max} , which is close to the melting point (1986 K) of SiO₂⁷. In addition, silicon monoxide (SiO) may gradually form at high T via a decomposition reaction, $\text{SiO}_2 + \text{Si} \rightleftharpoons 2 \text{SiO}$; SiO is volatile and can evaporate away by sublimation⁸.

As an example, Fig. 1a, b reveal time–temperature profiles $T(t)$ measured by the radiation pyrometer for the cycles #1 and #10. The sample temperature T given here was calibrated using Wien's law: $1/T = 1/T_p + (1/T_l - 1/T_{lp})$, where T_p is the pyrometer signal and T_{lp} is the pyrometer signal at the liquidus temperature. In the beginning of the cycle the temperature reading of the solid sample rises quickly and reaches a plateau corresponding to the solidus temperature T_s (1383 K), where the sample starts to melt. The $T(t)$ -profile approaching T_s shows no significant disturbances, indicating that in spite of a low electric conductivity the highly doped semiconductor can be well positioned in the EML facility. Because of the lower emissivity of the liquid, the temperature reading $T(t)$ drops down during melting and subsequently reaches a minimum, which corresponds to the actual liquidus temperature T_l . The large fluctuation ($\Delta T \approx 200$ K) of the $T(t)$ -profile in the two phase region arises from the different spectral emissivity of the solid (0.48) and the liquid (0.22) read by the pyrometer depending on the actual spot. The small fluctuation ($\Delta T \approx 50$ K) is due to

¹I. Physikalisches Institut, Georg-August-Universität, D-37077 Göttingen, Germany. ²Institut für Materialphysik im Weltraum, Deutsches Zentrum für Luft- und Raumfahrt (DLR), D-51170 Köln, Germany. ✉email: yluo@gwdg.de

Table 1. Overview of melting cycles performed for the sample $\text{Si}_{50}\text{Ge}_{50}$, including achieved overheat and undercooling as well as averaged cooling rates measured undercooling gas (350 mbar Ar).

Cycle	SCE	Pulses	Axial/radial camera (Hz)	Overheat (K)	Undercooling (K)	Averaged cooling rates ($T > T_l/T < T_l$) (K s^{-1})
#1	–	–	50/400	378	35	36/19
#2	–	–	50/400	365	40	35/20
#3	On	–	50/400	385	50	34/16
#4	On	–	50/400	355	35	31/12
#5	–	4×	150/400	357	55	30/13
#6	–	4×	150/400	366	155	29/10
#7	–	4×	150/400	380	200	30/7.5
#8	–	4×	150/400	375	190	30/7.8
#9	–	2×	150/400	390	200	28/7.8
#10	–	2×	150/400	390	205	29/7.5
#11	On	–	50/400	380	240	28/6

SCE is a sample coupling electronics used to determine inductively the sample resistivity (see Fig. 7).

changes in view factor caused by movement of the sample. During melting the sample becomes metallic, so that the force applied by the electromagnetic levitation field on the droplet grows and improves its positioning stability. As a consequence, the $T(t)$ -profile in liquid state appears very smooth. Figure 1c, d is the video image of the sample obtained at the beginning of solidification from cycle #1 and #10. These show a strongly heterogeneous and a more homogeneous nucleation at the surface corresponding to small and large undercooling degrees indicated in Fig. 1a, b, respectively. The strongly heterogeneous nucleation is accompanied by a dendritic growth (Fig. 1c) and emerges mainly in cycles #1–#5, where residual SiO_2 oxide impurities on the surface serve likely as a nucleus for solidification. Because of a low height of free energy barrier, the heterogeneous nucleation is in general more common than homogeneous nucleation.

The rather homogeneous nucleation occurs for the first time in cycle #6, where the undercooling degree jumps up with no observable dendrite structure (Fig. 1d). The phenomenon can be contributed to the absence of the oxide impurities, which are obviously molten or evaporated during the processing in the first cycles, followed by a rise in undercooling (Table 1) in the subsequent cycles. Because of the homogeneous coverage of nuclei on the sample surface, the $T(t)$ -profile now appears smooth at the beginning of the solidification and rises due to the exothermic nature of the process. The growth of the nuclei is accompanied by a volume expansion (volume anomaly⁶) and as a result, the liquid inside is partly pressured out, forming a bump on the surface. For this case, the $T(t)$ -profile fluctuates regularly up and down upon the sample rotation.

Oscillating drop method

Figure 2 shows typical axial and radial images measured for $\text{Si}_{50}\text{Ge}_{50}$ at different points indicated in the relevant $T(t)$ -profile in Fig. 2a. The artefacts stem from parts of the sample holder. The areas were excluded in the edge fitting procedure, yielding data of areas A and lengths of horizontal and vertical radii R_1 and R_2 as well as elliptical semiaxes a and b , used for evaluation of thermophysical properties via the oscillating drop method. To minimize errors, we introduce an average radius R calculated from R_1 , R_2 , a , b and r_{eff} , where r_{eff} is an effective radius extracted from the area $A = \pi r_{\text{eff}}^2$. The normalized areas A/A_0 and radii R/R_0 with A_0 and R_0 denoted as their mean values are plotted in Fig. 2a, showing damped oscillations caused by switching off the electromagnetic heating field, which also squeezes the droplet, and short voltage pulses.

As illustrated in Fig. 2c, the short pulse squeezes the drop into a prolate shape along the perpendicular axis. The cross-section viewed from the top in axial direction becomes correspondingly small and in radial direction looked incomplete due to a hiding effect of the magnetic coil (its winding distance is 8 mm). The uniaxially deformed droplet relaxes to its equilibrium spherical shape, giving rise to surface oscillations. A similar behavior appears at T_{max} by turning off the heating. In this case the uniaxial deformation is however much stronger than that induced by short pulses, giving rise to rotation of the droplet around an arbitrary axis with a period of about 1 Hz (see Fig. 3b). The overlap between rotation and oscillation makes the droplet temporarily aspherical (Fig. 2b) and lead to extra scattering of the experimental data (Fig. 5a). Only far away from heating-off or pulses, the droplet becomes quiet and well spherical, as shown in Fig. 2d. For this case, all length data R_1 , R_2 , a , and b are nearly identical and the scattering becomes smaller (Fig. 5b).

Viscosity of the droplet

Typical oscillations of the levitated $\text{Si}_{50}\text{Ge}_{50}$ droplet excited at different T by start off and on heating pulses are presented as a function of the time t in Figs. 2a and 3a, b. The amplitude decays exponentially with t and approaches then the mean value A_0 (or R_0). The behavior can be fitted by $f = f_0 \pm \Delta f e^{-\lambda t}$, here f/f_0 is denoted as A/A_0 or R/R_0 , Δf as their maximal amplitude. The fit provides the envelope of the oscillation as plotted in Fig. 3a, b (dashed line) and yields a matched decay factor λ , which can be referred as the magnitude of the viscosity, i.e. $\eta = \kappa \lambda^9$. Here the constant $\kappa = \frac{3M}{20r_0} = 12.8 \text{ mPa s}^2$ is calculated with $M = 1.07 \text{ g}$ and $r_0 = 4 \text{ mm}$.

The dashed lines in Fig. 3a illustrate the envelopes matched to oscillations (axial data of cycle #10) excited by heating off at 1940 K (T_{max}) and two short pulses at 1480 and 1380 K. The relevant decay factors λ are found to be 0.25, 0.5, and 0.68 s^{-1} , respectively, showing a temperature dependence. Figure 3b shows the oscillation of the droplet caused by heating off only (radial data of cycle #2). The impact from the rotation is visible. It creates a parasitic oscillation of about 1 Hz and disturbs the observation of the decay behavior, giving rise to additional errors. The dashed lines in Fig. 3b (upper part) present the fits with exponential function of $e^{-\lambda t}$, while the solid line in Fig. 3b (bottom) is simply obtained by linear fitting of the natural logarithm $\ln |A/A_0 - 1|$. Both calculations yield the same decay constant λ . In this case 0.3 s^{-1} by fitting the data up to $t = 8 \text{ s}$.

Figure 3c gathers the damping factors λ of the oscillating droplet $\text{Si}_{50}\text{Ge}_{50}$ at different T from data of cycles #1 to #11. They

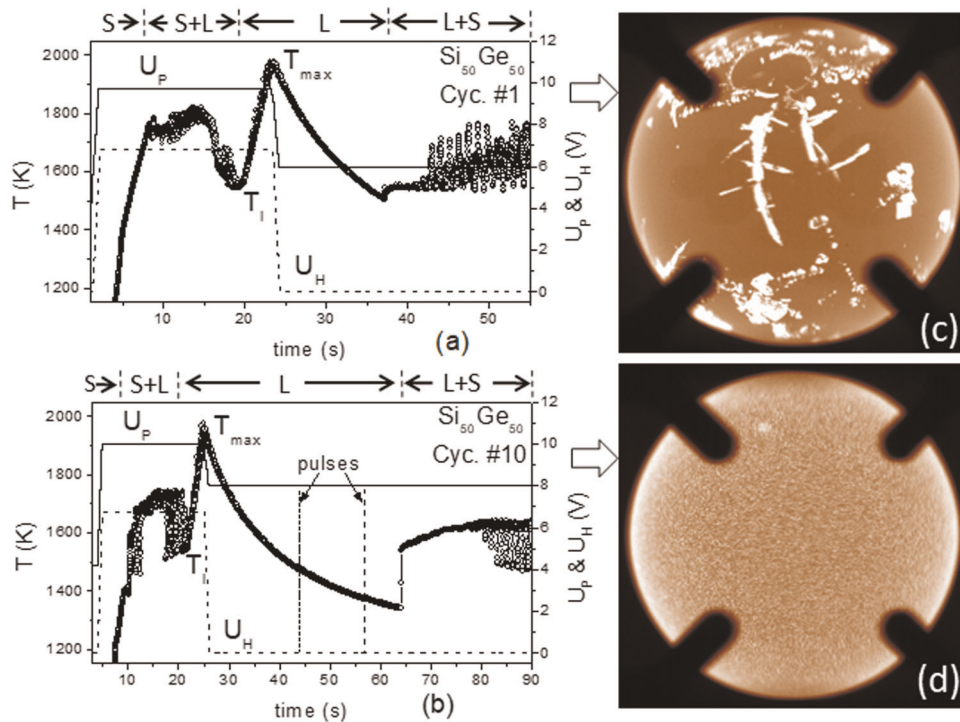


Fig. 1 Time–temperature profiles (circles) measured for $\text{Si}_{50}\text{Ge}_{50}$. **a** from cycle #1 and **b** from cycle #10, showing a small and a large undercooling, respectively. Solid and dashed lines show the voltages U_P and U_H controlling the electromagnetic fields for positioning and heating of the sample. **b** shows two pulses used for excitation of drop oscillations. **c** and **d** are images of the sample recorded at beginning of the solidification, showing strongly heterogeneous and more homogeneous nucleation at the surface associated with small and large undercooling shown in **(a)** and **(b)**.

are lower than the values measured in parabola flights⁶ and only weakly temperature dependent. Note the oscillation of cycle#1–#4 and #11 is excited by heating-off at T_{\max} only. The relevant decay constant λ was found to be within 0.15–0.31 s^{-1} (circles in Fig. 3c) and averaged at 0.23, which would correspond to a saturation value η of about 3.0 mPa s at high T . λ rises then slightly with decreasing T , passing through T_I without a remarkable change. At low T , it amounts to about 0.6 s^{-1} , corresponding to η of about 8 mPa s.

For a discussion of the viscosity data measured here by the oscillating drop method the fluid flow in the sample plays a crucial role. In EML experiments even the positioning field in the cooling phase can lead to turbulent flow and therefore to an enhanced viscosity¹⁰. Qualitatively, the turbulent behavior can be observed by the movements of oxide particles, which exist on the surface in the first five cycles. Particles of about 50–100 μm in size could be tracked in the radial video images. They circulate or move chaotically on the droplet surface with maximum observed velocities v of about 0.12 m s^{-1} . The Reynolds number Re , which is defined as the ratio of inertial force $\frac{\rho v^2}{L}$ to viscous force $\frac{\eta v}{L^2}$ (ρ is the density of the droplet and L its characteristic dimension), i.e. $Re = \frac{\rho v L}{\eta}$ ¹¹, can be estimated to be $Re \geq 5700$, taking $\rho = 5.9 \text{ g cm}^{-3}$, $L = 8 \text{ mm}$ (diameter of the sample) and the viscosity η assumed to be $\leq 1 \text{ mPa s}$ as measured in experiments with an electrostatic levitator (ESL), where no turbulence should occur^{10,12,13}. The high Re value of the $\text{Si}_{50}\text{Ge}_{50}$ droplet causes the flow instability and turbulent flow occurs.

An additional indication for the turbulent flow is the dynamical behavior of the surface of the melt showing self-excited oscillations during the whole cooling phase. For doped Ge, which is used in another EML-experiment, fluid flow modeling resulted in high Reynolds numbers of about 6500–70,000 indicating highly

turbulent flow within the droplet in the whole temperature range¹⁴.

These findings lead to the conclusion that the measured damping factor λ may be dominated by the levitation force induced fluid flow and as a result, the relevant η may deviate from the molecular viscosity measured in other experiments on earth. The argumentation is supported by the smaller value of $<1 \text{ mPa s}$ measured for Si in an ESL by Zhou et al.¹² and Li et al.¹³. In contrast to an EML, the levitation force does not drive convection in an ESL. For previous EML experiments on parabola flights with Ge-rich Si-Ge-samples⁶, we measured viscosity data of about 5–10 mPa s at high temperatures, higher than the actual values measured on ISS, which may be caused by very high positioning fields necessary in parabola flights and therefore enhanced fluid flow.

In addition, the molecular viscosity η may be estimated roughly by its relation to the surface tension γ as suggested by Egly¹⁵ and Brillo¹⁶, namely $\frac{\gamma}{\eta} = 0.94 \sqrt{\frac{RT}{W}}$. With the molar gas constant $R = 8.314 \text{ J mol}^{-1} \text{ K}^{-1}$, the molecular weight $W = 50.35 \text{ g mol}^{-1}$ of $\text{Si}_{50}\text{Ge}_{50}$ and a measured value $\gamma = 0.6 \text{ N m}^{-1}$ near T_I (cf. Fig. 4a) we get a value η of about 1.2 mPa s in accordance with the measured values discussed. In principle, this form provides an opportunity to separate the temperature dependence of the damping into turbulent and laminar flow. On the other hand it should be noted that the relation derived by Egly is not strictly applicable for $\text{Si}_{50}\text{Ge}_{50}$. It is only valid for pure elements and simple metallic liquids and should only be used for an estimate of the order of magnitude for the viscosity.

Surface tension of the droplet

To determine the surface tension γ of the droplet $\text{Si}_{50}\text{Ge}_{50}$, the frequency spectra were deduced by fast Fourier transform (FFT) of the oscillation data. Figure 4a exhibits the frequency spectra obtained from the droplet oscillations excited by short pulses at 1810, 1645, and 1415 K, respectively, exhibiting a resonance peak

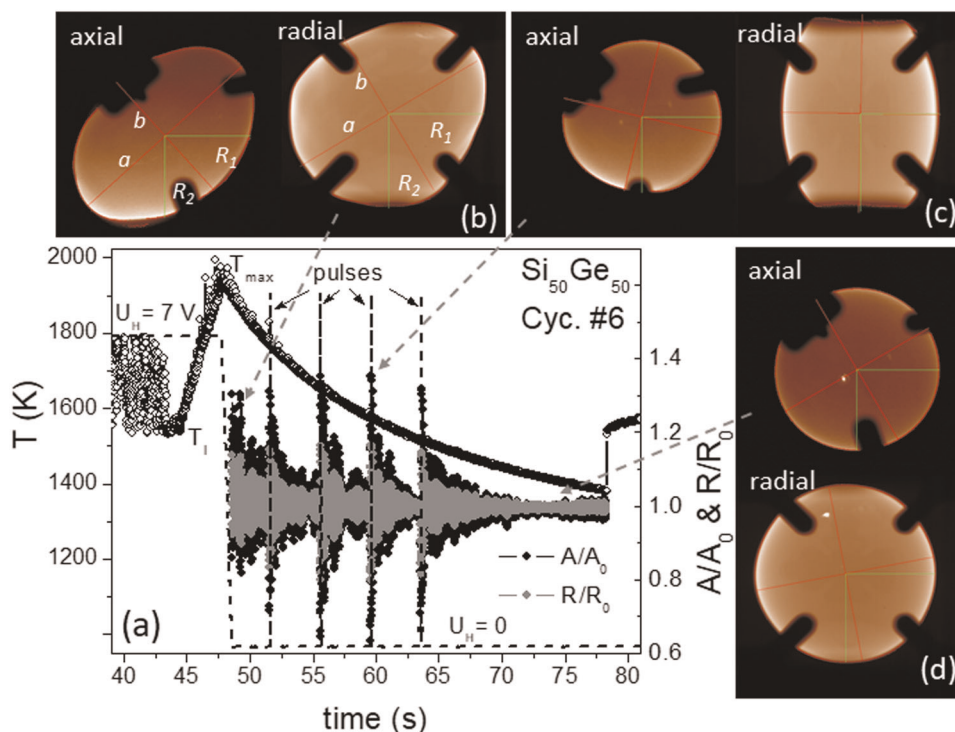


Fig. 2 Time profiles and sample images of cycle #6. **a** Gives temperature (circles), voltage U_H (dashed line) controlling the electromagnetic heating field with four short pulses used for exciting droplet oscillations, as well as normalized areas A/A_0 (black) and radii R/R_0 (gray). Relevant axial and radial images of the sample captured between heating-off and the first pulse (**b**), at the third pulse (**c**), and far away from the fourth pulse (**d**), respectively, involving elliptical semiaxes a , b (red), horizontal and vertical radii R_1 , R_2 (green) as well as areas A surrounded by edge curves.

located at $\nu = 22$ Hz and its higher harmonic peaks. A temperature dependence is here visible; the resonance peaks are shifted towards higher frequency for decreasing temperature. Since γ is a function of ν , namely $\gamma = \xi\nu^2$ (ref. ⁹) with $\xi = \frac{3\pi M}{8}$ (M is the droplet mass), this result implies an increase of γ . Parasitic oscillations arising essentially from the rotation of the droplet (~ 1 Hz) are overlapped with the surface oscillation, leading to splitting of the resonance peaks (detailed see the inset in Fig. 4a, b) and have to be taken into account by the evaluation of the resonance frequency.

To minimize the impact from the parasitic oscillations, we have to operate the FFTs segmentally using a series of time segmentations, s_1, s_2, \dots as schematically illustrated in Fig. 4b. By means of a careful division, a data segmentation yields a frequency spectrum with a single resonance peak (though it may appear somehow slightly asymmetrical). A series of γ values as a function of the temperature were extracted in this manner and are plotted versus T in Fig. 4c (where dashed lines are drawn in view of the average). The results in Fig. 4c (upper part) are from the cycles #1–#4 and #11 (without additional pulses), in which the droplet oscillations are induced by heating-off at T_{\max} (cf. Fig. 3b) and driven by turbulent flow over whole temperatures until $T < T_l$. Since the surface resonance selects natural frequency of the droplet¹⁰, the self-excited oscillation enables the measurements of the surface tension in the whole T range with similar results obtained from the pulse cycles #5–#10 (see Fig. 4c, lower part).

In addition to the errors caused by splitting or asymmetrical behavior of the resonance peak regarding the droplet rotation, the deformation of the droplet may give rise to a frequency shift, as recently investigated by Xiao et al.¹⁷, using a molten nickel-based superalloy with a deformation amplitude δ up to 7%. They gave an equation, $\frac{\Delta\nu}{\nu} = p_1\delta + p_2\delta^2$, to describe the deformation induced frequency shift. Since the constant p_1 and p_2 are negative, the frequency shifts towards lower values. This nonlinear behavior is

also visible here and even pronounced at the beginning of excited oscillations as indicated by arrows in Fig. 4c (lower part). The deformation amplitude δ of the molten $\text{Si}_{50}\text{Ge}_{50}$ can be estimated from the R/R_0 data shown in Figs. 2 and 3a. It is about 15% at the beginning of the excited oscillations and decreases rapidly with t . After 1 or 2 s, $\delta < 10\%$. The δ value is somewhat above the limit reported in ref. ¹⁷. Nevertheless, the equation mentioned is valid for a qualitative discussion. An influence from oxide contamination (a few separated tiny particles) is insignificant, though it causes a small undercooling in the cycles #1–#5.

The measured surface tension is comparable to published data in the literature. In previous parabola flight experiments with undoped Si–Ge samples¹⁸ and doped Si–Ge samples with rich Ge content⁶, the values and the temperature dependences are similar. Measurements with an ESL also lie in the same range¹³. Experiments with the pendant drop method on earth show similar values¹⁹.

Thermal expansion

Figure 5a shows the normalized A/A_0 and R/R_0 for the cycle #1. Largely scattered data beyond 1 ± 0.2 for A/A_0 (1 ± 0.1 for R/R_0) arising from strong deformations of the droplet during the heating-off period (about 1 or 2 s) were removed. Since T is here mostly above T_l , the data represent behaviors of the overheated liquid. Figure 5b shows the data obtained from the deeply undercooled liquid (cycle #11 without a pulse). Due to a small deformation of droplet the scattering of the data is much smaller (1 ± 0.02), compared with those given in Fig. 5a.

Linear fitting these data yields coefficients $\beta_A = A^{-1} dA/dT$ ($A = \text{area}$) and $\beta_R = R^{-1} dR/dT$ ($R = \text{radius}$) of area and linear thermal expansion in given temperature ranges. The error values in brackets shown in Fig. 5a, b give the uncertainty of the linear fit. As expected, β_A is found here to be nearly equal to $2\beta_R$. More interestingly, we found the coefficients ($\beta_A = 10.0 \times 10^{-5} \text{ K}^{-1}$ and

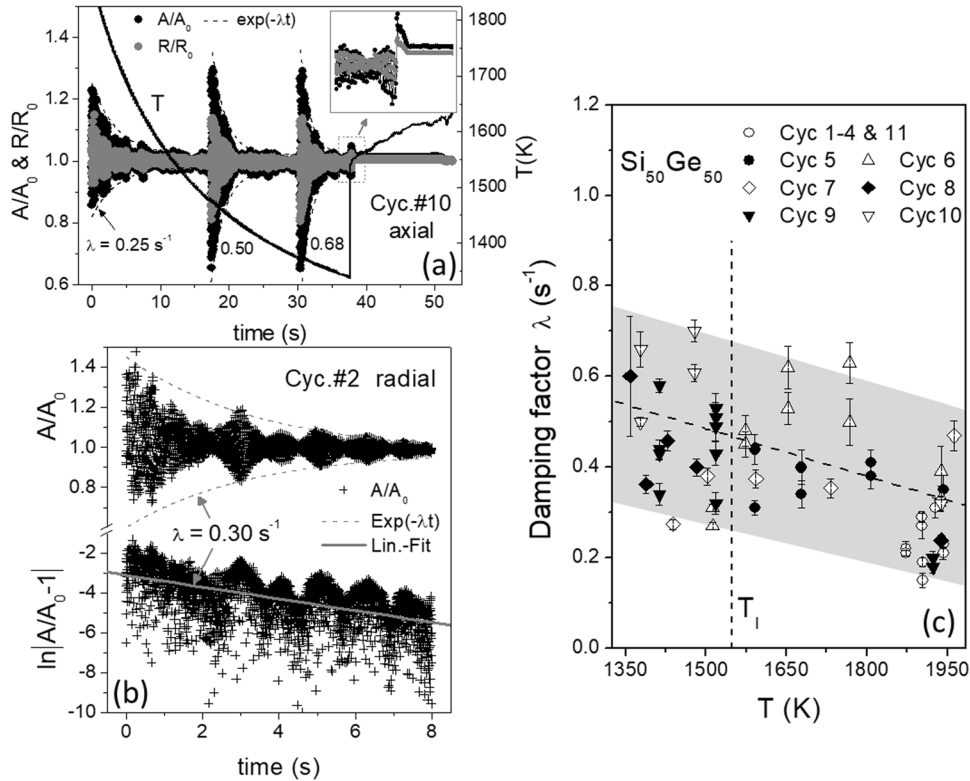


Fig. 3 **a** $T(t)$ profile of the cycle #10 with normalized axial areas A/A_0 (black) and radii R/R_0 (gray), revealing oscillations excited by heating-off and short pulses respectively and decayed with t in an exponential function $e^{-\lambda t}$ (dashed lines), as well as abrupt changes occurring upon solidification (inset) regarding volume anomaly⁶. **b** (upper) Decayed oscillations of radial A/A_0 from cycle #2 excited by heating-off, showing an extra low period of ~ 1 Hz caused by droplet rotations, (bottom) linear fitting of $\ln|A/A_0 - 1|$ to get the decay constant λ . **c** Damping factors λ of the oscillations measured for 11 cycles. A linear fit gives $\lambda = 0.5 - 3.5 \times 10^{-4}(T - T_1) \text{ s}^{-1}$ (dashed line). The gray background indicates the scattering of $\pm 0.2 \text{ s}^{-1}$. The weak T dependence is probably due to the influence of the turbulent flow effect.

$\beta_R = 4.9 \times 10^{-5} \text{ K}^{-1}$) obtained from the highly overheated melt (Fig. 5a), being much higher than those ($4.25 \times 10^{-5} \text{ K}^{-1}$ and $2.14 \times 10^{-5} \text{ K}^{-1}$) obtained from the deeply undercooled one (Fig. 5b). The result suggests a nonlinear thermal expansion of the liquid.

To show this in more detail, Fig. 5c exhibits relevant axial and radial video data, covering both overheating and undercooling temperature ranges. Note that the radial data of cycle #11 is combined here with the radial data of cycle #3, due to the limited data storage capacities on board the ISS and thus a restricted length (≤ 30 s) of radial image video data (400 Hz). In addition, to minimize the scattering the data plotted in Fig. 5c were smoothed by adjacent averaging. A nonlinear behavior of the droplet size with T is apparent, which can approximately be fitted by a second-degree polynomial as is demonstrated in Fig. 5c. The polynomial has the form

$$\begin{aligned} R/R_0 &= a_R + \beta_{R_0}(T - T_0) + \beta'_R(T - T_0)^2 \text{ and} \\ A/A_0 &= a_A + \beta_{A_0}(T - T_0) + \beta'_A(T - T_0)^2 \end{aligned} \quad (1)$$

with constant $a_{R,A}$ close to 1. By differentiation of the Eq. (1), we get the thermal expansion coefficient as a linear function of T , namely

$$\beta_{R,A} = \beta_{R,A0} + 2\beta'_{R,A}(T - T_0) \quad (2)$$

with $\beta_{R,A0} \approx 10^{-5} \text{ K}^{-1}$ as initial value at T_0 and $2\beta'_{R,A} \approx 10^{-7} \text{ K}^{-2}$ as the slope (see Fig. 5d). With the help of the Eq. (2), the β_R value at the melting point T_1 can be evaluated. Averaging over the cycles #1–#5, we get a mean β_R of $3.40 \times 10^{-5} \text{ K}^{-1}$. It appears larger than that ($2.90 \times 10^{-5} \text{ K}^{-1}$) averaged over cycles #6–#11, which, in contrast to the cycles #1–#5, possess more data of the deeply undercooled and spherical droplet. The difference arises therefore,

on the one hand, from fitting errors depending on the data precision, but on the other hand, it mirrors again the nonlinear behavior of the thermal expansion. The mean value β_R of $3.15 \times 10^{-5} \text{ K}^{-1}$ averaged using the values from all cycles represents the linear expansion coefficient of the $\text{Si}_{50}\text{Ge}_{50}$ melt near T_1 . It, although partly contributed from deep undercooled melt, appears slightly above the value of $\beta_R = 3.0 \times 10^{-5} \text{ K}^{-1}$ measured by previous parabola flight experiments for overheated pure Ge (1275–1675 K)⁶. The result implies an impact of the composition. For the nonlinear term in the Eq. (1) we found $2\beta'_A = 2.43 \times 10^{-7} \text{ K}^{-2}$ and $2\beta'_R = 1.25 \times 10^{-7} \text{ K}^{-2}$ from the slopes in Fig. 5d. Again, a factor of ≈ 2 is found for β'_A/β'_R (see above).

The density of the melts of Si and Ge was measured by a thermometric method by Glazov and Shcelikov²⁰ about 20 years ago. They also found a nonlinear temperature dependence of the thermal expansion and discussed this behavior in terms of a decrease in the strength of interatomic bonds with increasing temperature. The experimental results are comparable to the behavior of the Si–Ge melts investigated here in the ISS-EML.

Kulkarni et al.²¹ performed ab initio MD simulations of Ge melts. They argue that at lower temperatures the structure factor shows a pronounced shoulder on the high k -side of the principal peak, which vanishes for high temperatures consistent with experimental scattering data in the literature. The coordination number increases with increasing temperature. This behavior of the structure factor is accompanied by an angle distribution function showing some tetrahedral arrangements at lower temperatures as well.

Following Kulkarni et al.²² our interpretation of the temperature dependence of the volume of the Si–Ge melt states that at very

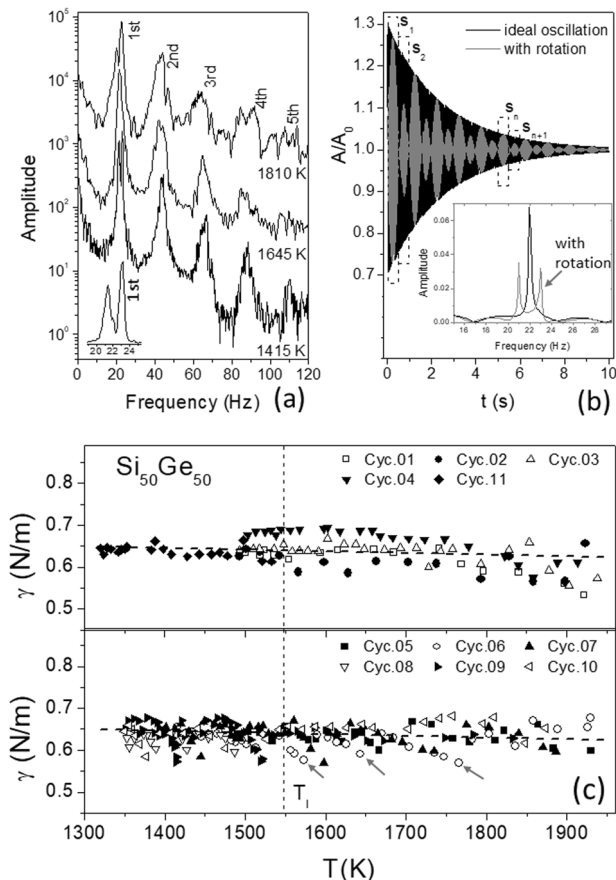


Fig. 4 **a** Frequency spectra obtained from droplet oscillations induced by short pulses at 1810, 1645, and 1415 K, respectively. **b** Simulation of oscillations without and with droplet rotation. **c** Surface tension γ obtained (upper) from the cycles #1–#4 and #11, (bottom) from pulse cycles #5–#10, the lower values are indicated by arrows (here only for cycle #6) associated with relatively high droplet deformations at the beginning of excited oscillations.

high temperatures the melt behaves like a simple metallic melt where a linear thermal expansion is expected²². With decreasing temperature, covalent, tetrahedral structure elements (small range order) begin to form and therefore the specific volume deviates from that of a simple liquid, which is characterized by a simple two body interatomic potential with linear thermal expansion, leading to the observed nonlinear temperature dependence.

In addition, the solidification of the melt is accompanied with an abrupt increase in A/A_0 and R/R_0 as illustrated in the inset of Fig. 3a. The phenomenon can be partly contributed to the volume expansion due to T rise, and partly to the volume anomaly of the substances Si and Ge, whose density in solid is lower than that in liquid⁶.

Electrical resistivity of the droplet

The temperature-dependent electrical resistivity $\rho(T)$ is a sensitive indicator for structural changes in the melt. Generally, the electrical resistivity in liquid metals results from the scattering of the conduction electrons at the disordered metal ions. Accordingly, the decline of the temperature dependent density fluctuations in the melt with decreasing temperature results in the usually observed linear decrease of ρ ²². In liquid alloys a formation of compact structures (clusters) with decreasing temperature, due to chemical short-range ordering processes of the components, may result in an increase of the scattering cross-section for the electrons and thus of the electrical resistivity²³. Consequently, an

onset of clustering phenomena in a liquid alloy may lead to a deviation of $\rho(T)$ from the typical linear temperature dependence. The lower the temperature of the melt is the more pronounced this effect should show up.

This above assumption is confirmed by the present liquid Si₅₀Ge₅₀ sample. Figure 6 shows a plot of the resistivity data against the temperature measured during the cooling phase of cycle #11, where the undercooling of the liquid Si₅₀Ge₅₀ droplet was very high (cf. Figure 1b and Table 1).

Assuming that the Si₅₀Ge₅₀ melt can be considered as a regular solution with a positive heat of mixing $W^{Si,Ge} > 0$ ²⁴, meaning, that external heat is necessary to keep the liquid alloy components mixed, the unusual temperature behavior of the electrical resistivity can be described by the physical model of Takeuchi and Endo²³

$$\rho^{Si,Ge}(x_{Si}, x_{Ge}, T) = \rho_0^{Si,Ge}(x_{Si}, x_{Ge}) + \rho_1^{Si,Ge}(x_{Si}, x_{Ge}) \cdot T + \frac{\rho_2^{Si,Ge}(x_{Si}, x_{Ge})}{1 - 2x_{Si}x_{Ge}W^{Si,Ge}/RT} \quad (3)$$

with x_{Si} and x_{Ge} denoted as the concentrations of Si and Ge (presently $x_{Si} = x_{Ge} = 1/2$), $\rho_0^{Si,Ge}(x_{Si}, x_{Ge})$, $\rho_1^{Si,Ge}(x_{Si}, x_{Ge})$ and $\rho_2^{Si,Ge}(x_{Si}, x_{Ge})$ as temperature-independent constants. Corresponding to the conventional resistivity model, the Eq. (3) contains a constant term and a term which is linearly dependent on the temperature T . The last term finally considers the increase of the electrical resistivity with decreasing T due to the assumed increasing component demixing tendency in the melt, as discussed above. A weighted fit to the measured data points with $\rho_0^{Si,Ge} = 1.9 \times 10^{-5} \Omega \text{ cm}$, $\rho_1^{Si,Ge} = 2.2 \times 10^{-8} \Omega \text{ cm K}^{-1}$, $\rho_2^{Si,Ge} = 1.6 \times 10^{-5} \Omega \text{ cm}$, and $W^{Si,Ge} = 12 \text{ kJ mol}^{-1}$ is shown in the diagram of Fig. 6. Even if the demixing assumption is too simple to explain the real structural development in the undercooled Si₅₀Ge₅₀ melt, Eq. (3) describes at least phenomenologically the measured temperature-dependent electrical resistivity of the Si₅₀Ge₅₀ melt fairly well. The structural evolution of the deeply undercooled Si₅₀Ge₅₀ melt may be also influenced by a liquid–liquid phase transition of the Si component and the reinforcement of its tetrahedral order^{25,26}.

METHODS

EML facility and sample description

The experiments were performed in the microgravity electromagnetic levitator ISS-EML on board the International Space Station (ISS). The facility applies two superposed, radio frequency electromagnetic fields on electrically conducting samples in its center (see Fig. 7). A quadrupole-like “positioning field” (150 kHz), generated by two oppositely directed RF coil currents, to containerlessly confine a liquid droplet at a dedicated place against external residual forces, and a homogeneous dipole-like “heating field” (400 kHz), generated by two RF coil currents in the same direction, to efficiently heat and melt the sample inductively.

Although originally designed for metallic materials only, the low residual forces in the microgravity environment enable processing of highly doped semiconductors in the facility. A more detailed description of the levitation principle can be found in ref. 27. For visual observation of the samples two high-resolution CCD-cameras are installed. An axial camera with a frame rate of 50 Hz (resolution 704 × 704 pixels) or 150 Hz (resolution 352 × 352 pixels) looking from the top along the symmetry axis of the magnetic fields on the sample. This camera is combined with a pyrometer for temperature measurements. A radial camera with a frame rate of 400 Hz and a resolution of 600 × 600 pixels is looking from the side on the sample. More details of the facility can be found in ref. 28.

The spherical Si₅₀Ge₅₀ sample used has a mass of $M = 1.07 \text{ g}$ and a radius of $r_0 = 4 \text{ mm}$. The raw material stems from a highly doped alloy crystal prepared by the Czochralski technique in the group of Abrosimov²⁹ at the IKZ Berlin. The dopant is boron (B) with a concentration of about $1.9 \times 10^{20} \text{ atoms cm}^{-3}$, which corresponds to an electrical conductivity of about $1.7 \times 10^3 \Omega^{-1} \text{ cm}^{-1}$ at 300 K. Due to the semiconducting behavior, the conductivity of the solid sample grows with T and jumps up to about

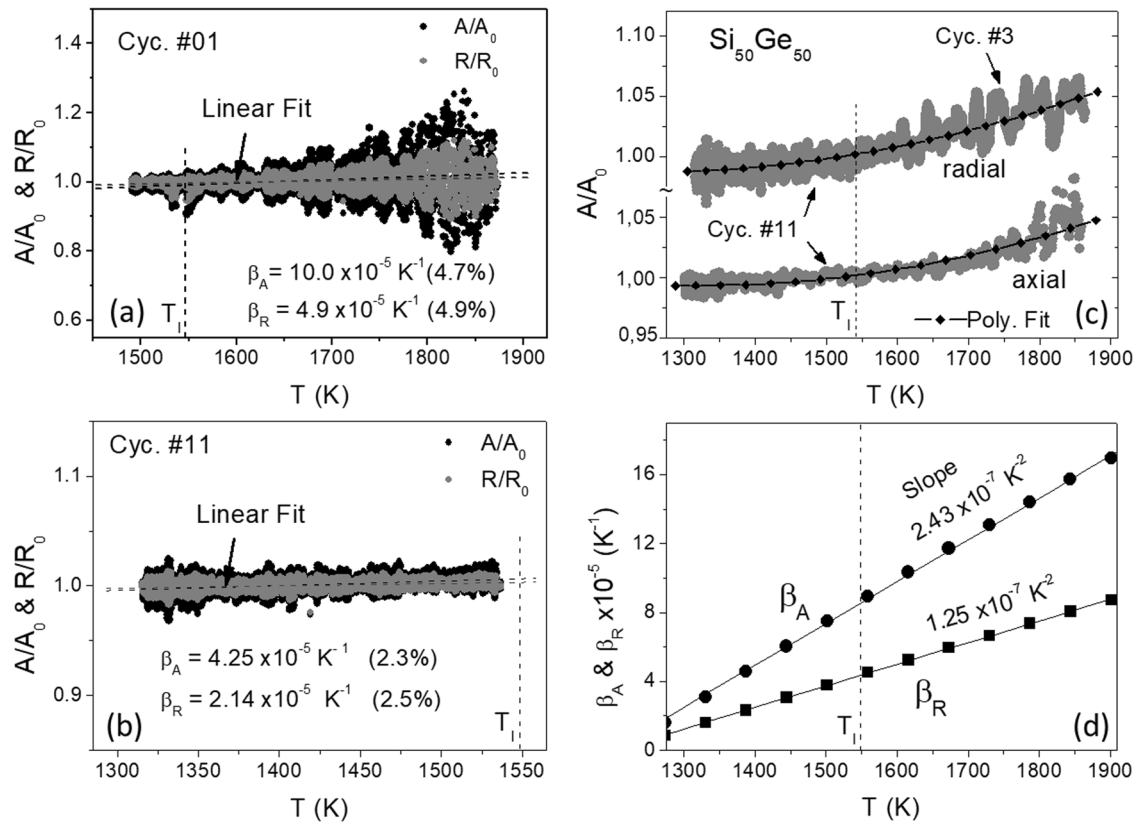


Fig. 5 Normalized areas A/A_0 and radii R/R_0 measured as a function of T for $\text{Si}_{50}\text{Ge}_{50}$. **a, b** Radial data from cycle #1 and #11. **c** (bottom) Axial data from cycle #11 and (top) radial data from cycles #3 and #11, showing a nonlinear behavior, which can be fitted by a second-order polynomial. **d** Thermal expansion coefficients β_A (area) and β_R (radius) as a function of T with a slope in the order of magnitude of about 10^{-7}K^{-2} .

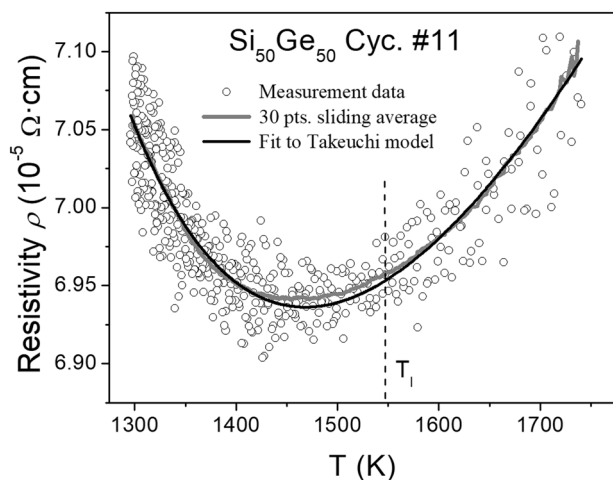


Fig. 6 Inductively measured electrical resistivity data (circles) of the $\text{Si}_{50}\text{Ge}_{50}$ melt for different temperatures above the melting point and in the undercooled regime. The curve (black) is a fit of the resistivity model of Takeuchi and Endo²³ to the data points, which agrees fairly well with the sliding average over 30 data points (grey line).

$10^4 \Omega^{-1} \text{cm}^{-1}$ (corresponding to a resistivity of about $10^{-4} \Omega \text{cm}$ as given in Fig. 6) upon melting regarding to the semiconductor–metal phase transition caused by disordering.

The sample concentration was checked/confirmed by EDX analyses. The liquidus temperature T_l at 1548 K and solidus temperature T_s at 1383 K are taken from the literature³⁰.

Ground test and parabola flight experiments

Relevant ground tests were made in advance by the Microgravity User Support Center (MUSC) at DLR, Cologne, Germany, to obtain the data of spectral emissivity ϵ required for the pyrometer, sample-coil coupling efficiency and the evaporation rate of the melt regarding the limits of dust generation. The measured spectral emissivity ϵ is 0.48 for the solid and 0.22 for the liquid phase. The inductive coupling efficiency is actually a measure for processability of the semiconductor sample in EML and was used for simulation of the planned melting cycles in ISS-EML. The coupling in the solid phase was found to be strong enough for a fast heating of the sample. In the liquid state, the sample is metallic and the coupling becomes enhanced by a factor of about 5.

The processability of highly doped semiconductors was verified by parabolic flight experiments provided by ESA and the DLR Institute of Material Physics in Space on board a Zero-G aircraft operated by Novespace, France using the similar EML setup TEMPUS⁵. The results indicated that the samples could be heated up in the solid phase, melted and positioned stable in liquid phase. Unfortunately, due to the short experiment time (~ 20 s) available and a relatively high T_l of the $\text{Si}_{50}\text{Ge}_{50}$ sample, only preliminary experiments could be performed.

ISS experimental details

Before the transport to ISS, the sample was cleaned with acetone and ethanol in ultrasound bath and integrated in a special transport container which was pumped down to 10^{-7} mbar and filled then with 1 bar Ar. During the end inspection, the sample was exposed to air and it is expected that the surface is covered with a natural thin passivation oxide layer, which prevented the sample from further oxidation.

The ISS experiments were performed during the vibration-free astronaut sleep period with 11 cycles (Table 1), consisting of heating and melting to maximal temperatures of up to $T_{\text{max}} \sim 1925$ K and cooling down below T_s , as shown in Figs. 1a, b and 2a. At T_{max} the heater was dimmed to its idle state, i.e. the heater control voltage was set to $U_H = 0$ and the positioner control voltage U_p decreased accordingly by about 2–3 V. During the

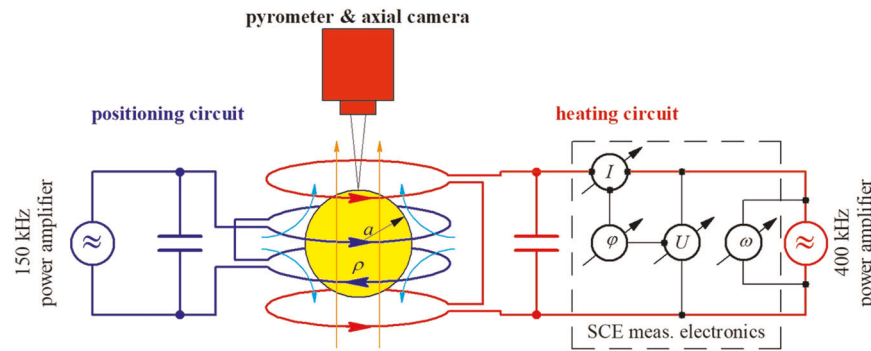


Fig. 7 Principal sketch of the electrical oscillating circuits of the microgravity levitation facility ISS-EML including the quadrupole-like RF electromagnetic positioning field (cyan), and the homogeneous dipole-like RF electromagnetic heating field (orange). The corresponding electrical circuits are powered by their own current supply. The actual EML circuits, basing on the superposition principle, differ in details from those shown above. The SCE electronics, used to determine inductively the temperature-dependent sample resistivity and dimension, is hooked up to the heating circuit.

following cooling phase, within which the disturbances by the electromagnetic force fields are just lowest, the different experiments with the sample were executed in an Argon gas atmosphere (350 mbar), which was necessary for a reduction of the evaporation rate (mass loss) of the overheated melt. A cycle took typically 1–2 min depending on the undercooling degree of the melt. A mass loss of about 0.1–0.2 mg per cycle was estimated from the evaporation experiments performed by MUSC as well as from the experience of the parabola flight experiments.

The surface tension γ and viscosity η of the melt were determined by the oscillating drop technique^{9,28}. For this purpose, short pulses (triangle, 8 V, 0.05 s) in the heating field were set at different temperatures T in cycles #5–#10 (Figs. 1b, 2a, and 3a). The pulse squeezes the drop into a prolate shape along the heating field and results in damped surface oscillations to its equilibrium spherical shape. The exponential decay constant λ of the oscillation amplitude gives the viscosity of the sample, i.e. $\eta = \kappa\lambda$ with the proportional constant $\kappa = \frac{3M}{20\pi r_0}$ (M is the mass and r_0 is the radius of the sample), while the resonance frequency ν , which can be extracted from the fast Fourier transform (FFT) of the oscillation data, yields the surface tension $\gamma = \xi\nu^2$ with $\xi = \frac{3\pi M}{8}$ (refs. 9,31). Unfortunately, the relaxation of the deformed drop is accompanied by a translational movement and a rotation (~ 1 Hz) of the droplet, which disturb the evaluation of the oscillation behavior and create extra scattering of the data. To minimize this disturbance, the melting cycles #1–#4 and #11 were done without pulses (cf. Table 1). However, at high temperatures near T_{\max} the oscillation caused by switching off the heating field is unavoidable, leading to a large scatter of image data in this regime. The droplet oscillations were monitored by the axial and radial video cameras and its images were analyzed with respect to the above described oscillating drop method using a dedicated software “TeVi” (SEA Datentechnik GmbH), which detects the edges of the sample from the image contrast. The edge curve is fitted with a polynomial of degree 9 (ref. 32) and yields areas, radii, and semiaxes of the droplet. From these data also the thermal expansion coefficients β of the sample could be determined.

The electrical resistivity of the liquid $\text{Si}_{50}\text{Ge}_{50}$ droplet is measured inductively. For this purpose the homogeneous radio frequency (RF) magnetic heating field can very well be used. This field, generated by an RF current I of angular frequency ω in the heating coil (see Fig. 7) induces eddy currents in the material, the strength of which depends on the electrical resistivity of the droplet. These eddy currents in turn generate an RF magnetization field depending on the resistivity and dimension of the sample. It induces an additional voltage U backwards in the coil, the strength and phase shift φ (relative to the current I) of which is determined by a dedicated measurement electronics (SCE). The data are monitored with a rate of 10 Hz and with a resolution of 16 Bit, for details see ref. 27.

DATA AVAILABILITY

The datasets generated and analyzed during the current study are available from the corresponding author upon reasonable request.

Received: 1 November 2019; Accepted: 3 March 2020;

Published online: 25 March 2020

REFERENCES

- Cressler, J. D. & Niu, G. *Silicon-Germanium Heterojunction Bipolar Transistors* (Artech House, Boston, London, 2002).
- King, R. R., Karam, N. H., & Haddad, M. Multijunction photovoltaic cells and panels using a silicon or silicon-germanium active substrate cell for space and terrestrial applications. US Patent US 6340788 B1 (2002).
- Currie, M. T. et al. Carrier mobilities and process stability of strained Si n - and p -MOSFETs on SiGe virtual substrates. *J. Vac. Sci. Technol.* **B19**, 2268–2279 (2001).
- Tanaka, T. et al. Upper limit of two-dimensional hole gas mobility in strained Ge/SiGe heterostructures. *Appl. Phys. Lett.* **100**, 222102 (2012).
- 25th DLR Parabolic flight campaign, 20th–31st October 2014, Practical and Technical Information, DL-2014-ed1-en, Novespace, Bordeaux-Mérignac, Mars 2014. See also www.novespace.com.
- Luo, Y. et al. Contactless processing of SiGe-melts in EML under reduced gravity. *NPJ Microgravity* **2**, 1–9 (2016).
- Haynes, W. M. (ed.). *CRC Handbook of Chemistry and Physics* 92nd edn. (CRC Press, Boca Raton, FL, 2011).
- Wiberg, E., Wiberg, N. & Holleman, A. F. *Inorganic Chemistry* (Academic Press, San Diego; De Gruyter, Berlin, New York, 2001).
- Egry, I., Lohöfer, G., Seyhan, I., Schneider, S. & Feuerbacher, B. Viscosity of eutectic Pd78Cu6Si16 measured by the oscillating drop technique in microgravity. *Appl. Phys. Lett.* **73**, 462–463 (1998).
- Hyers, R. W. Fluid flow effects in levitated droplets. *Meas. Sci. Technol.* **16**, 394–401 (2005).
- Reynolds, O. An experimental investigation of the circumstances which determine whether the motion of water shall be direct or sinuous, and of the law of resistance in parallel channels. *Philos. Trans. Roy. Soc. Lond.* **174**, 935–982 (1883).
- Zhou, Z., Mukherjee, S. & Rhim, W. K. Measurement of thermophysical properties of molten silicon using an upgraded electrostatic levitator. *J. Cryst. Growth* **257**, 350–358 (2003).
- Li, J. J. Z., Rhim, W. K., Kim, C. P., Samwer, K. & Johnson, W. L. Evidence for a liquid–liquid phase transition in metallic fluids observed by electrostatic levitation. *Acta Mat.* **59**, 2166–2171 (2011).
- Bracker, G., et al. *12th International Workshop on Subsecond Thermophysics (IWSSSTP 2019)*, 3–6 June 2019, Cologne, Germany.
- Egry, I. On the relation between surface tension and viscosity for liquid metals. *Scr. Met. Mat.* **26**, 1349 (1992).
- Brillo, J. *Thermophysical Properties of Multicomponent Liquid Alloys* (DE Gruyter Oldenbourg, Walter de Gruyter GmbH, Berlin/Boston, 2016).
- Xiao, X., Hyers, R. W., Wunderlich, R. K., Fecht, H. J. & Matson, D. M. Deformation induced frequency shifts of oscillating droplets during molten metal surface tension measurement. *Appl. Phys. Lett.* **113**, 011903 (2018).
- Chathoth, S. M., Damaschke, B., Samwer, K. & Schneider, S. Thermophysical properties of Si, Ge, and Si–Ge alloy melts measured under microgravity. *Appl. Phys. Lett.* **93**, 071902 (2008).
- Ricci, E. et al. Surface tension and density of Si–Ge melts. *J. Chem. Phys.* **140**, 214704 (2014).

20. Glazov, O. V. & Shchelikhov, M. D. Volume changes during melting and heating of silicon and germanium melts. *High Temp.* **38**, 405–412 (2000).
21. Kulkarni, R. V., Aulbur, W. G. & Stroud, D. Ab initio molecular-dynamics study of the structural and transport properties of liquid germanium. *Phys. Rev. B* **55**, 6896 (1997).
22. Takeuchi, S. & Endo, H. The electric resistivity of the metals in the molten state. *Trans. JIM* **3**, 30–35 (1962).
23. Takeuchi, S. & Endo, H. Theoretical and experimental studies on the resistivity of molten alloys. *Trans. JIM* **3**, 35–41 (1962).
24. Olesinski, R. W. & Abbaschian, G. J. Ge-Si (Germanium-Silicon) system. *Bull. Alloy Phase Diagr.* **5**, 180–183 (1984).
25. Krishnan, S. et al. The structures of normal and supercooled liquid silicon metal and SiGe alloy. *J. Non-Cryst. Solids* **353**, 2975–2981 (2007).
26. Jakse, N. et al. Structural changes on supercooling liquid silicon. *Appl. Phys. Lett.* **83**, 4734–4736 (2003).
27. Lohöfer, G. High-resolution inductive measurement of electrical resistivity and density of electromagnetically levitated liquid metal droplets. *Rev. Sci. Instrum.* **89**, 124709 (2018).
28. Seidel, A., Soellner, W. & Stenzel, C. EML—an electromagnetic levitator for the International Space Station. *J. Phys. Conf. Ser.* **327**, 012057 (2011).
29. Abrosimov, N. V., Rossolenko, S. N., Thieme, W., Gerhardt, A. & Schröder, W. Czochralski growth of Si- and Ge-rich SiGe single crystals. *J. Cryst. Growth* **174**, 182–186 (1997).
30. Stohr, H. & Klemm, W. Über Zweistoffsysteme mit Germanium. I. Germanium/aluminium, germanium/zinn und germanium/silicium. *Z. Anorg. Allgem. Chem.* **241**, 305–323 (1939).
31. Brillo, J., Lohöfer, G., Schmidt-Hohagen, F., Schneider, S. & Egly, I. Thermophysical property measurements of liquid metals by electromagnetic levitation. *Int. J. Mat. Prod. Tech.* **26**, 247–273 (2006).
32. Keren, D. & Gotsman, C. Fitting curves and surfaces with constrained implicit polynomials. *IEEE Trans. Pattern Anal. Mach. Intell.* **21**, 31–41 (1999).

ACKNOWLEDGEMENTS

The authors acknowledge the access to the ISS-EML, which is a joint undertaking of the European Space Agency (ESA) and the DLR Space Administration. The reported work was conducted in the framework of the ESA research project SEMITHERM (AO-2000-068). The authors acknowledge also the colleagues from DLR/MUSC in Cologne for the help with the realization of the experiments and N. Abrosimov et al. in Leibniz Institute for Crystal Growth in Berlin for sample material preparations. The work is financially supported by DLR Bonn via project 50WM1750.

AUTHOR CONTRIBUTIONS

Experiment performance, data analysis and evaluations, as well as the manuscript preparation were done by Y.L., B.D., and G.L.; experiment idea and design and discussions of results by B.D., G.L., and K.S. All authors read, edited, and approved the final manuscript.

COMPETING INTERESTS

The authors declare no competing interests.

ADDITIONAL INFORMATION

Supplementary information is available for this paper at <https://doi.org/10.1038/s41526-020-0100-5>.

Correspondence and requests for materials should be addressed to Y.L.

Reprints and permission information is available at <http://www.nature.com/reprints>

Publisher's note Springer Nature remains neutral with regard to jurisdictional claims in published maps and institutional affiliations.



Open Access This article is licensed under a Creative Commons Attribution 4.0 International License, which permits use, sharing, adaptation, distribution and reproduction in any medium or format, as long as you give appropriate credit to the original author(s) and the source, provide a link to the Creative Commons license, and indicate if changes were made. The images or other third party material in this article are included in the article's Creative Commons license, unless indicated otherwise in a credit line to the material. If material is not included in the article's Creative Commons license and your intended use is not permitted by statutory regulation or exceeds the permitted use, you will need to obtain permission directly from the copyright holder. To view a copy of this license, visit <http://creativecommons.org/licenses/by/4.0/>.

© The Author(s) 2020